

Contribution of x-ray incident position dependence to energy resolution of Ti/Au transition-edge sensors

Qing-Xiao Ma(马卿效), Wen Zhang(张文), Pei-Zhan Li(李佩展), Zhi-Fa Feng(冯志发), Xian-Feng Zhou(周先锋), Zheng Wang(王争), Jia-Qiang Zhong(钟家强), Wei Miao(缪巍), Yuan Ren(任远), Jing Li(李婧), and Sheng-Cai Shi(史生才)

Citation: Chin. Phys. B, 2026, 35 (**3**): 038501. DOI: 10.1088/1674-1056/adfbd6
http://cpb.iphy.ac.cn; http://iopscience.iop.org/cpb

What follows is a list of articles you may be interested in

Transition-edge sensors using Mo/Au/Au tri-layer films

Hubing Wang(王沪兵), Yue Lv(吕越), Dongxue Li(李冬雪), Yue Zhao(赵越), Bo Gao(高波), and Zhen Wang(王镇)
Chin. Phys. B, 2023, 32 (**2**): 028501. DOI: 10.1088/1674-1056/ac7f94

Improvement of energy resolution of x-ray transition-edge sensor using K-means algorithm and Wiener filter

Qingxiao Ma(马卿效), Wen Zhang(张文), Peizhan Li(李佩展), Zheng Wang(王争), Zhifa Feng(冯志发), Xinkai Yang(杨心开), Jiaqiang Zhong(钟家强), Wei Miao(缪巍), Yuan Ren(任远), Jing Li(李婧), and Shengcai Shi(史生才)
Chin. Phys. B, 2023, 32 (**10**): 108501. DOI: 10.1088/1674-1056/acd7d4

Novel layout design of 4H-SiC merged PiN Schottky diodes leading to improved surge robustness

Jia-Hao Chen(陈嘉豪), Ying Wang(王颖), Xin-Xing Fei(费新星), Meng-Tian Bao(包梦恬), and Fei Cao(曹菲)
Chin. Phys. B, 2023, 32 (**9**): 098505. DOI: 10.1088/1674-1056/acad6b

Transition-edge sensors using Mo/Au/Au tri-layer films

Hubing Wang(王沪兵), Yue Lv(吕越), Dongxue Li(李冬雪), Yue Zhao(赵越), Bo Gao(高波), and Zhen Wang(王镇)
Chin. Phys. B, 2023, 32 (**2**): 028501. DOI: 10.1088/1674-1056/ac7f94

Temperature and current sensitivity extraction of optical superconducting transition-edge sensors based on a two-fluid model

Yue Geng(耿悦), Pei-Zhan Li(李佩展), Jia-Qiang Zhong(钟家强), Wen Zhang(张文), Zheng Wang(王争), Wei Miao(缪巍), Yuan Ren(任远), and Sheng-Cai Shi(史生才)
Chin. Phys. B, 2021, 30 (**9**): 098501. DOI: 10.1088/1674-1056/ac11ce

---

Contribution of x-ray incident position dependence to energy resolution of Ti/Au transition-edge sensors

Qing-Xiao Ma(马卿效)[1,2], Wen Zhang(张文)[1,†], Pei-Zhan Li(李佩展)[1], Zhi-Fa Feng(冯志发)[1,2], Xian-Feng Zhou(周先锋)[1,2], Zheng Wang(王争)[1], Jia-Qiang Zhong(钟家强)[1], Wei Miao(缪巍)[1], Yuan Ren(任远)[1], Jing Li(李婧)[1], and Sheng-Cai Shi(史生才)[1,‡]

[1] *Purple Mountain Observatory, Chinese Academic of Sciences, Nanjing* 210023, *China*
[2] *University of Science and Technology of China, Hefei* 230026, *China*

(Received 7 June 2025; revised manuscript received 18 July 2025; accepted manuscript online 15 August 2025)

We present the contribution of x-ray incident-position dependence on the absorber to the energy resolution of Ti/Au transition-edge sensors (TESs). The pulse height varies with the position due to insufficient thermal conductivity and geometry of the absorber that degrades the measured energy resolution. We develop a three-dimensional (3D) electro-thermal simulation model and thoroughly study the position dependent contribution to energy resolution ($\Delta E_{\rm p}$) for two presentative absorber structures: an absorber directly deposited on the center of TES sensor (design A) and an absorber cantilevered on the TES sensor by several stems (design B). For design A with a 30 μm×40 μm Au absorber $\Delta E_{\rm p}$ is found to be 9.4 eV, while it is reduced to 1.35 eV for design B with a 100 μm×100 μm Au absorber. Although the contribution of position dependence is relatively small, this study facilitates further optimization of the absorber structure to achieve enhanced energy resolution.

Keywords: transition-edge sensors, electro-thermal simulation, position dependence, energy resolution

PACS: 85.25.Oj, 85.25.Am, 72.15.Jf

DOI: 10.1088/1674-1056/adfbd6 **CSTR:** 32038.14.CPB.adfbd6

1. Introduction

Transition edge sensors (TESs), with extremely high energy resolution (ΔE) as calorimeter and sensitivity as bolometer, are detectors of choice in diverse fields including x-ray spectroscopy,[1] dark matter detection,[2] and astrophysics.[3] As a thermal detector, TES, operating on the sharp resistive transition of superconducting materials near the critical temperature ($T_{\rm C}$), enables high-precision signal transduction.[4] For example, Ti/Au bilayer TES microcalorimeter exhibits a ΔE of 2.0 eV at 5.9 keV.[5] To absorb the high-energetic particles, TES is usually coupled to a thin absorber made of high atomic number metals (i.e., Au and Bi) with high photon stopping power and quantum efficiency. Theoretical ΔE depends on the total heat capacity (C), which is mainly dominated by the large absorber. Due to the limited internal thermal conductivity, the pulse shape including its pulse height (PH) and rise-time ($\tau_{\rm el}$) varies with the incident position of the x-rays, which will degrade ΔE.[6] The effect of position dependence can be reduced by increasing the thermal conductivity of absorber.[7] We are developing TiAu-based x-ray TES with an Au absorber directly placed in contact with the TES sensor.[8] To reduce the thermal conductance (G), the silicon substrate underneath the TES sensor is etched[9] to form a membrane and the measured ΔE is about 100 eV at 5.9 keV, which is much higher than simulated one due to unknown excess noise. Besides the thermal fluctuation noise, Johnson noise and SQUID amplifier noise, the measured ΔE is further influenced by temperature stability, stray light as well as position dependence. We build an electro-thermal model with COMSOL Multiphysics software to study the position dependence and find that its contribution to the total ΔE is 9.40 eV. This contribution is further reduced to 1.35 eV for a cantilevered absorber structure (mushroom absorber).

2. Electro-thermal model

The temperature (T) in the TES follows the heat balance equation[10]

$$\rho c\frac{\partial T}{\partial t} = \nabla\cdot(k\nabla T) + Q_{\rm ext} + Q_{\rm joule}, \tag{1}$$

where ρ is the density, c is the specific heat, k is the thermal conductivity, $Q_{\rm ext}$ is the external heat source, and the joule heat ($Q_{\rm joule}$) can be described as

$$Q_{\rm joule} = J\cdot E, \tag{2}$$

here E is the electric field and J is the current density[11]

$$J = \sigma E + \frac{\partial D}{\partial t} + J_{\rm e}, \tag{3}$$

†Corresponding author. E-mail: wzhang@pmo.ac.cn
‡Corresponding author. E-mail: scshi@pmo.ac.cn

© 2026 Chinese Physical Society and IOP Publishing Ltd. All rights, including for text and data mining, AI training, and similar technologies, are reserved.

where σ is the electrical conductivity, D is the electric flux density, and J_e is the external current density.

The TES resistance (R) as a function of temperature (T) can be reproduced with an empirical formula[12]

$$R(T) = \frac{R_n}{2}\left[1 + \tanh\left(\frac{T - T_C}{\Delta T}\right)\right], \tag{4}$$

where R_n is the normal-state resistance and ΔT is the transition width, controlling the steepness and consequently the temperature sensitivity ($\alpha = T/R \times dR/dT$).

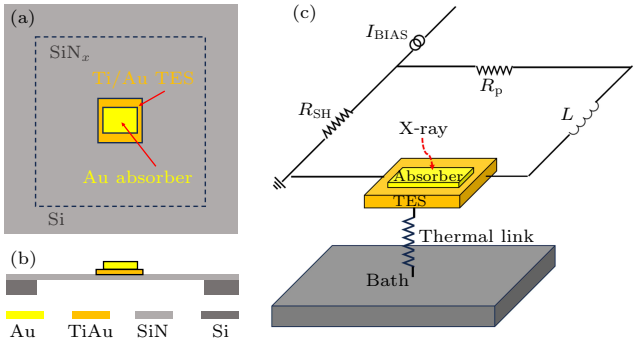


Fig. 1. (a) Top view and (b) cross-section view of the x-ray TES calorimeter. Au absorber and TiAu TES are 1.2-μm and 100-nm thick, respectively. Note that the thickness values are not in scale with the actual device for clarity. (c) The schematic diagram of the TES readout circuit. Shunt resistor (R_{SH}) and parasitic resistor (R_P) are both 2 mΩ, and the input coil (L) of the DC SQUID is 6 nH.

Table 1. Physical parameters of the TES calorimeter at cryogenic temperatures.[7,10]

Parameter		Value
TES	c_{TES} (J/(kg·K))	1.53×10^{-3}
	k_{TES} (W/(m·K))	1.66
	ρ_{TES} (g/cm^3)	14.77
Absorber	c_{Au} (J/(kg·K))	5.91×10^{-4}
	k_{Au} (W/(m·K))	4.57
	ρ_{Au} (g/cm^3)	19.32
SiN_x	c_{SiN_x} (J/(kg·K))	5.82×10^{-5}
	k_{SiN_x} (W/(m·K))	6.91×10^{-6}
	ρ_{SiN_x} (g/cm^3)	3.00
Si	C_{Si} (J/(kg·K))	7×10^{-6}
	k_{Si} (W/(m·K))	148
	ρ_{Si} (g/cm^3)	2.33

We first construct the whole structure of TiAu TES calorimeter with the Au absorber in contact with the TES sensor (called design A1). As shown in Fig. 1(a), the SiN_x membrane is 400 μm×400 μm, while the TES sensor and absorber are 50 μm×50 μm, and 30 μm×40 μm, respectively.[9] Figure 1(b) shows the cross-section view, and the thickness values of each layer are given. Note that the thickness is not in scale with the actual device for clarity. The physical parameters of all materials at cryogenic temperatures are taken from references[7,10] and listed in Table 1. The readout circuit is shown in Fig. 1(c). The TES is constant-voltage biased by applying a bias current (I_{bias}) to the 2-mΩ shunt resistor in parallel with the TES. Note that a 6-nH input coil (L) and a 2-mΩ parasitic resistor (R_P) are in series with the TES to simulate the actual circuit. Therefore, electro-thermal feedback is included in the simulation. The COMSOL software, based on finite-element method, can solve the electric circuit and thermal equations (Eqs. (1)–(3)) simultaneously. The current flowing through the TES (I_{TES}) is monitored by a virtual ampere meter. The Joule heat dissipated in the TES is taken into account with Eq. (4) as $P_{TES} = I_{TES}^2 R(T)$. During the simulation, the temperature at the membrane edges and bias current (I_{bias}) were set to 120 mK and 220 μA, which are consistent with the measurement condition.

3. Simulated results

We first simulate the steady-state temperature distribution of this whole device as shown in Fig. 2(a). The Joule heat generated in TES sensor is transferred to the heat sink via the weak SiN_x thermal links. Figure 2(b) shows the temperature distribution in the absorber. It is ∼ 190 mK and uniform due to good thermal conductivity of Au.

To simulate the pulse response, we replace the 5.9-keV x-ray irradiation with a heat source with a radius of 0.1 μm and duration of 10 ns. Figure 3 shows the simulated current pulse with a PH of 0.357 μA, which is in good agreement with the measured one.[9] The rise time (τ_{el}) and fall time (τ_{eff}) are 5.4 μs and 56 μs, respectively. We can conclude that the simulation is reliable as we adopt the actual physical parameters at cryogenic temperatures and the electric circuit includes R_P and L of DC SQUID.

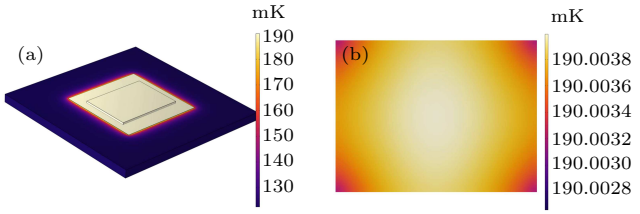


Fig. 2. (a) The steady-state temperature distribution of the whole device (A1), (b) temperature distribution in the absorber.

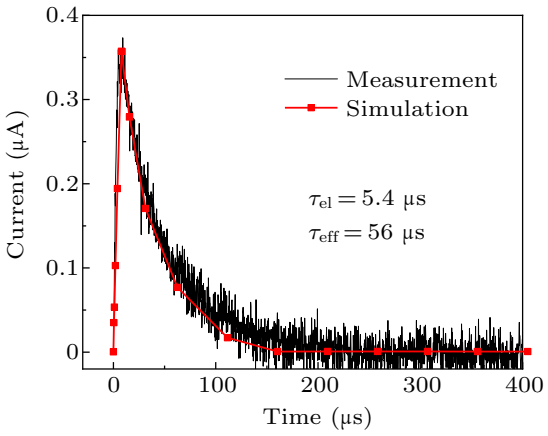


Fig. 3. A comparison of the simulated pulse and a measured typical pulse of A1 device. A heat source with an energy of 5.9 keV is injected at the center of the absorber.

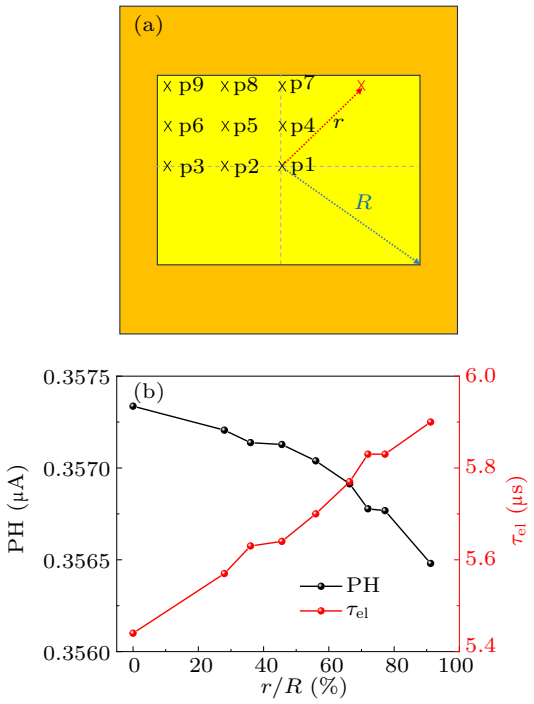


Fig. 4. (a) The heat injection points (p1–p9) on the absorber. r denotes the distance between the injection point to the center, and R is the maximum distance, (b) PH and τ_{el} as a function of the normalized distance (r/R) of device A1.

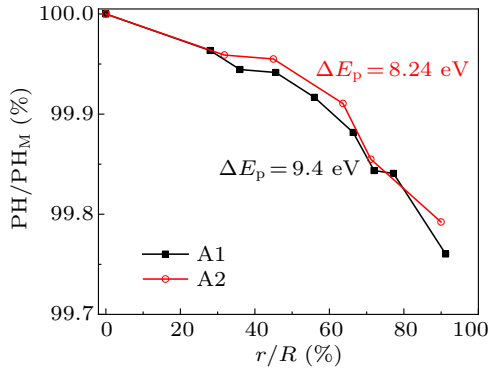


Fig. 5. PH as a function of normalized distance (r/R) for devices A1 and A2. The calculated contributions of position dependence to energy resolution are 9.4 eV and 8.24 eV, respectively.

We then investigate the position dependence of PH. As shown in Fig. 4(a), only 9 points (p1–p9) on the absorber are selected as the heat incident positions, thanks to the geometric symmetry of the TES calorimeter. The parameter r denotes the distance between the point to the center, and R is the maximum distance. Figure 4(b) shows the simulated PH as a function of distance normalized to R. It can be seen that PH gradually decreases with distance, while the rise time (τ_{el}) increases. Assuming the pulse height at the center corresponds to 5.9 keV, PH value at each point is then converted to energy. The energy's standard deviation (σ) is calculated with the assumption that x-rays should uniformly impinge on the absorber. The contribution of the position dependence to the energy resolution is $\Delta E_p = 2.355\sigma$. Although PH at the corner is close to the value in the center: 99.76%, ΔE_p is estimated to be 9.4 eV, much less than the measured ΔE of $\sim$ 100 eV. It indicates that the position-dependent contribution is relatively small.

To minimize the position effects, the absorber is changed to a square with a length of 40 μm (called design A2). The other parameters including physical parameter and geometry are kept unchanged. We repeat the simulation and plot the normalized PH as a function of normalized distance as shown in Fig. 5. PH at the corner reaches as high as 99.79% that in the center, and hence position-dependent contribution (ΔE_p) is reduced to 8.24 eV.

The thermal conductance (G) between absorber and TES sensor is good enough as the absorber is directly deposited on the TES sensor. The heat deposited into the absorber is quickly transferred to the TES sensor. However, if x-ray is incident at the corner, part of energy possibly escapes into the heat bath through the weak SiN_x membrane before heating the TES. We thus studied an alternative absorber structure: mushroom-type (design B).[13] As shown in Fig. 6, a large Au absorber is supported by 6 Au stems: 4 stems are anchored on the membrane and 2 stems on the TES sensor. These cylinder stems are 3 μm in diameter and 2 μm in height, and the absorber is 200 μm×200 μm (design B1).

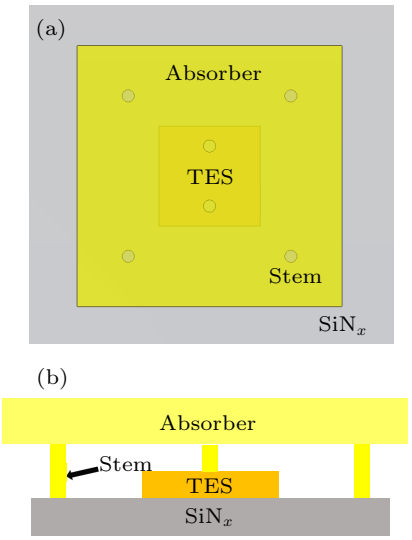


Fig. 6. (a) Top view and (b) cross-section view of the mushroom-type device (design B). Au absorber is supported by 6 Au stems: 4 stems are anchored on the membrane and 2 stems on the TES sensor.

In this case, the heat capacity is much larger than before, thus the temperature change is smaller as well as PH. As shown in Fig. 7(a), for the case that heat is injected at the center of absorber, τ_{el} and τ_{eff} of design B1 are 7.26 μs and 74 μs, which are slightly larger than design A1. There are three points with the same distance (i.e., 32%, 64%, and 71%), where the calculated PH is slightly different due to the asymmetry of two stems on the TES senser. In general, the pulse height exhibits uniform distribution: PH at the corner is 99.94% that at the center (see Fig. 7(b)). The contribution of position dependence is improved to 2.16 eV, which is much smaller than design A1.

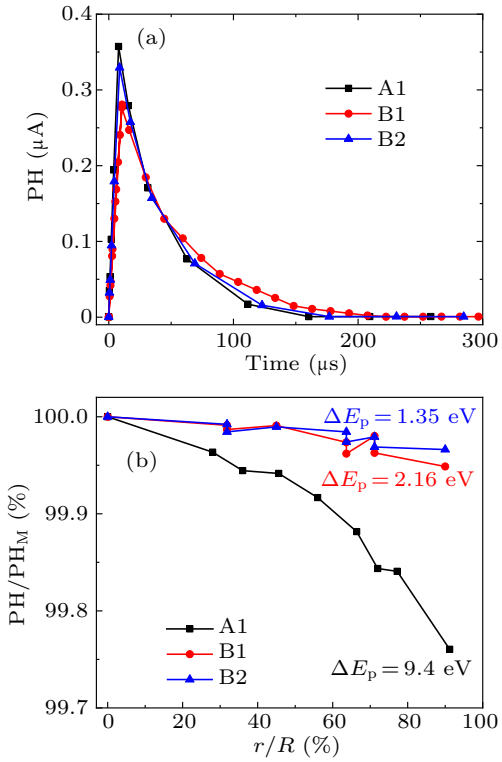


Fig. 7. (a) Simulated pulses with the heat source injected at the center of absorber for designs A1, B1, and B2. (b) The corresponding PH as a function of normalized distance. The position-dependent contributions to energy resolution are 9.4 eV, 2.16 eV, and 1.35 eV.

We further decrease the Au absorber to 100 μm×100 μm (design B2). The simulated current pulse is also plotted in Fig. 7(a) for comparisons. The PH of design B2 is increased to 0.329 μA thanks to a smaller thermal capacitance. For the same reason, τ_{el} and τ_{eff} are 6.11 μs and 62 μs, respectively. PH at the corner is further increased to 99.96% that at the center. The position-dependent contribution to energy resolution is further reduced to only 1.35 eV.

4. Conclusion and perspectives

We investigated the contribution of position dependence to the energy resolution of x-ray TESs by electro-thermal simulation with COMSOL software. The simulation model was first verified by measured pulse. By optimizing the absorber structure and size, the energy resolution degradation caused by position dependence was reduced to 1.35 eV. We will optimize our x-ray TESs to achieve better performance in the future.

Acknowledgements

Project supported in part by the National Key Research and Development Program of China (Grant No. 2023YFC2206600) and the National Natural Science Foundation of China (Grant Nos. 12293032 and 12020101002).

References

[1] Uhlig J, Doriese W B, Fowler J W, *et al.* 2015 *J. Synchrotron Rad.* **22** 766
[2] Paolucci F, Buccheri V, Germanese G, Ligato N, Paoletti R, Signorelli G, Bitossi M, Spagnolo P, Falferi P, Rajteri M and Gatti C 2020 *J. Appl. Phys.* **128** 194502
[3] Smith S J, Adams J S, Bandler S R, Beaumont S, Chervenak J A, Denison E V, Doriese W B, Durkin M, Finkbeiner F M, Fowler J W and Hilton G C 2021 *IEEE Trans. Appl. Supercond.* **31** 2100806
[4] Irwin K D and Hilton G C 2005 *Cryogenic Particle Detection* (Berlin: Springer) pp. 63–150
[5] Nagayoshi K, Ridder M L, Bruijn M P, Gottardi L, Taralli E, Khosropanah P, Akamatsu H, Visser S and Gao J R 2020 *J. Low Temp. Phys.* **199** 943
[6] Morgan K M, Busch S E, Eckart M E, Kilbourne C A and McCammon D 2014 *J. Low Temp. Phys.* **176** 331
[7] Ota R, Tanaka K, Hayashi T, Miyagawa R, Yagi Y, Yamasaki N Y and Mitsuda K 2024 *J. Low Temp. Phys.* **217** 366
[8] Ma Q X, Zhang W, Li P Z, Wang Z, Feng Z F, Yang X K, Zhong J Q, Miao W, Ren Y, Li J and Shi S C 2023 *Chin. Phys. B* **32** 108501
[9] Ma Q X, Zhang W, Wang Z, Li P Z, Feng Z F, Zhong J Q, Miao W, Ren Y, Li J and Shi S C 2025 *IEEE Trans. Appl. Supercond.* **35** 2101706
[10] Mori S, Nishida Y, Iyomoto N, Yagi Y, Konno R, Hayashi T, Tanaka K, Yamasaki N Y, Mitsuda K, Sato R and Saito M 2022 *J. Low Temp. Phys.* **209** 518
[11] COMSOL Multiphysics® *AC/DC Module User's Guide for COMSOL Multiphysics*® ver. 6.1 COMSOL Inc. 2023
[12] Burney J A 2007 *Transition-edge sensor imaging arrays for astrophysics applications* Ph.D. Dissertation (Stanford University)
[13] Zhao Y, Wang H, Gao B and Wang Z 2023 *Superconductivity* **7** 100051